ELSEVIER

International Journal of Thermal Sciences 41 (2002) 823–841

International Journal of Thermal Sciences

www.elsevier.com/locate/ijts

Detailed heat transfer measurements of impinging jet arrays issued from grooved surfaces

Lo May Su [1], Shyy Woei Chang *

Department of Marine Engineering National Kaohsiung Institute of Marine Technology Kaohsiung, Taiwan, ROC

Received 18 June 2001; accepted 25 October 2001

Abstract

Heat transfer augmentation of impinging jet-array with very small separation distances ($S/D_j < 1$) is attempted by using the grooved orifice plate through which the nozzles with different diameters are fitted. The combined effects of groove and nozzle-size distribution in an array have demonstrated considerable influences on heat transfers via their impacts on inter-jet reactions. With a specified coolant flow rate; the detailed heat transfer distributions over the impinging surfaces of three tested arrays are compared to reveal the optimal selections of separation distance and array configuration. Heat transfer modifications caused by varying jet Reynolds number (*Re*) and separation distance (S/D_j) over the ranges of $1000 \leqslant Re \leqslant 4000$ and $0.1 \leqslant S/D_j \leqslant 8$ are examined for each test array. In conformity with the experimentally revealed heat transfer physics, a regression-type analysis is performed to develop the correlations of spatially-averaged Nusselt numbers, which permit the individual and interactive effect of *Re* and S/D_j to be evaluated.

Keywords: Impinging jet-arrays

1. Introduction

An impinging jet-array could offer high convective capability that usually requires the large coolant flow rate with a small pressure drop, which condition is attainable in an electronic device facilitated with forced convective system. As an illustrative example, Fig. 1 depicts the customary cooling configuration and the conceptual design of an impinging jet-array cooling systems for the CPU of a personal computer. The thermal power of a CPU in general is in the range of 40–80 W with the area for dissipating heat of about 10 mm × 10 mm. This provides the heat flux of 400–800 $\mathrm{kW \cdot m^{-2}}$ which requires the effective cooling scheme to remain the operating temperatures at about 90 °C. As shown in Fig. 1(a) for the conventional cooling scheme, the CPU base is attached with a fin assembly over which a cooling fan that facilitates forced convection is installed. The complete assembly is normally vertically installed in the board of a personal computer so that the earth gravity is directed downward. An alternative design concept, which employs the impinging jet-array cooling scheme, issues the jets from an orifice plate as shown in Fig. 2(b). The spent fluid after impingement is radially convected over the CPU base. For the available total coolant consumption facilitated by the fan unit, the mass flux issued from each jet in the orifice plate varies due to the locally variant pressure field established over the impinging surface. The differences in the mass flux between the jets in an array are functionally related with the geometrical features of the jet-array system and the total coolant flow rate. Its consequential effects on the heat transfer distributions over the impinging surface have to be simulated and considered during the phase of devising the heat transfer correlations for engineering applications. Such thermal treatment for high heat dissipation electronic components could employ both laminar and turbulent jet-arrays. The complexities involved in an impinging jet-array physically relate to the jet entrainment, jet-to-jet interference, crossflow, wall-jet flow transition and the structures of turbulence and vorticity in the flows. For design application, their impacts on heat transfer are customarily described as functions of separation distance and jet Reynolds number for a set of geometrical specifications. Based on previous experimental results [1–5], Lee and Vafai [6] developed a

* Correspondence and reprints.
E-mail address: swchang@mail.nkimt.edu.tw (S.W. Chang).
[1] Department of Electrical Engineering Tong Fang College of Technology and Commerce.

1290-0729/02/$ – see front matter
PII: S1290-0729(02)01377-7

Nomenclature

D_j	diameter of jet nozzle for baseline array .... m	S	separation distance ..... m
k_f	thermal conductivity of fluid ..... $W{\cdot}m^{-1}{\cdot}K^{-1}$	T_j	fluid temperature at exit of nozzle ..... °C
H	jet-to-jet space ..... m	T_f	film temperature $= (T_w + T_j)/2$ ..... °C
Gr	area-averaged Grashof number of jet-array	T_w	wall temperature ..... °C
$\dot{M}$	total mass flow rate issued from jet-array ..... $kg{\cdot}s^{-1}$	u_c	cross flow velocity ..... $m{\cdot}s^{-1}$
M_j	coefficients	u_j	jet velocity ..... $m{\cdot}s^{-1}$
Nu	local Nusselt number $= q D_j/k_f(T_w - T_j)$	X, Y	dimensionless location $(x/D_j, y/D_j)$
Nu_a	area-averaged Nusselt number of jet-array region	*Greek symbols*	
Nu_c	area-averaged Nusselt number of central jet region	β	thermal expansion coefficient of coolant .. K^{-1}
q	convective heat flux ..... $W{\cdot}m^{-2}$	μ	fluid dynamic viscosity ..... $kg{\cdot}m^{-1}{\cdot}s^{-1}$
Re	Reynolds number $= \frac{4}{9\pi}\frac{\dot{M}}{D_j\mu}$	ρ	fluid density ..... $kg{\cdot}m^{-3}$
		$\Phi_{1,2}$	functions
		Δ	represents a difference

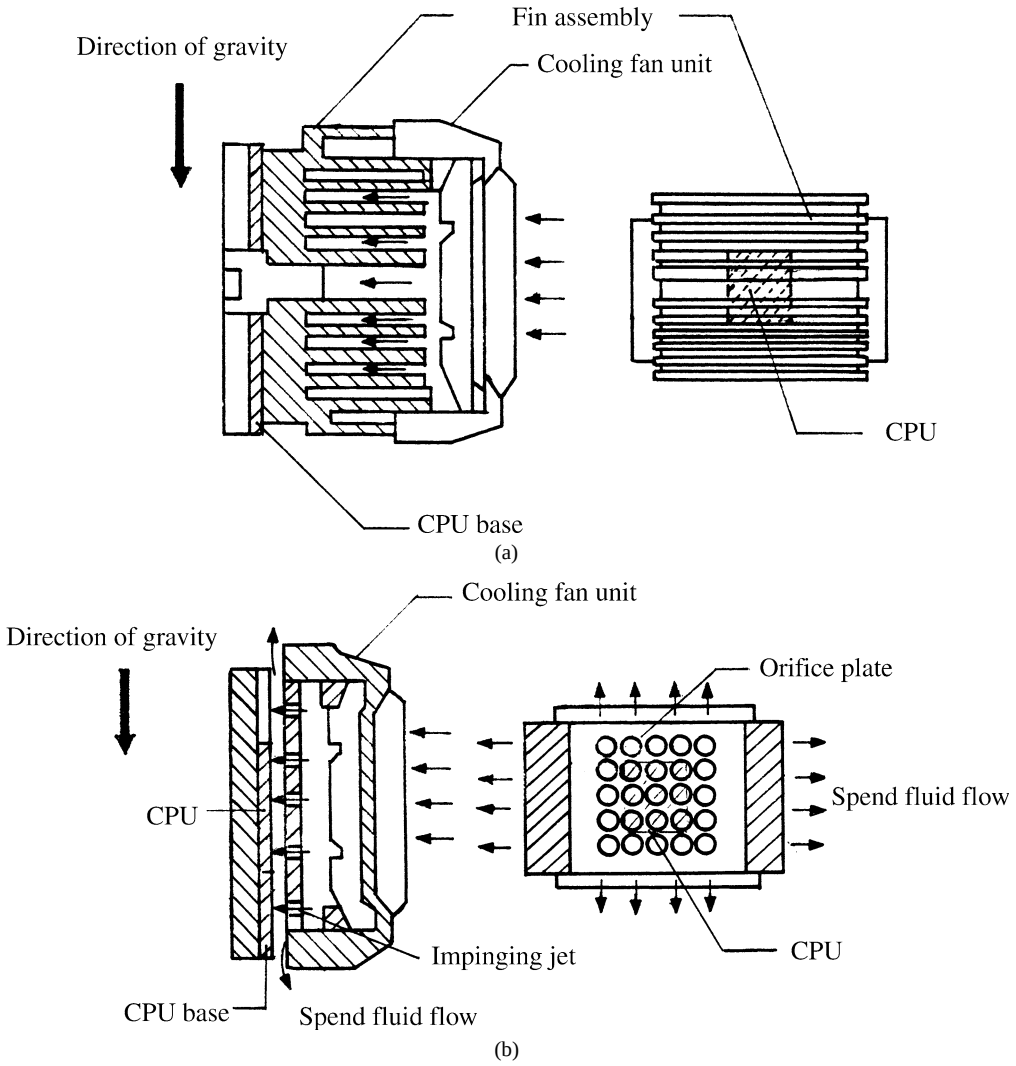

Fig. 1. Conceptual diagrams of cooling systems for CPU of personal computer: (a) Typical cooling geometry of CPU. (b) Conceptual impinging jet-array cooling geometry of CPU.

procedure to determine the optimal separation and nozzle-to-nozzle distances for an impinging jet-array. The maximum convective capability attainable with the impinging jet-array is significantly affected by the manner of treating the spent flow [6]. Because the spent fluid is forced to flow laterally over the impinging surface, the outlet stream of the spent fluid forms the crossflow that could deflect or diffuse the momentum of free jet. With condition of $\frac{S}{D_j}\frac{u_c}{u_j} > 0.1$, the crossflow effect is not negligible [1–6]. Heat transfer is generally deteriorated by the crossflow but might be enhanced due to the crossflow itself when S/D_j is very small [4,6–9]. This crossflow effect depends on the direction of exit spent-flow in a confined system [10]; but is minimized by locating the spent air exits through the openings in the impinging surface or in the nozzle plate [11–13]. The effectiveness of these additional spent air exits increases with the decrease of jet-to-jet spacing since it minimizes both the jet-to-jet interference and crossflow degradation [12,13]. Such favorable treatment of spent flow, however, may not be feasible when it becomes inadequate to allocate the openings through the impinging surface or the orifice plate. The other measure to assist the transportation of radial spent fluid is thus considered. In this respect, the introduction of grooves on the orifice plate may be an alternative solution to assist the convection of spent fluid from the inter-jet region and its impact on heat transfer has to be investigated.

Over the impinging surface, the networks along which the radial spent fluid is convected form the hexagonal and square webs, respectively, for the staggered and in-line jet-arrays [14]. The development of such radial network is a result of jet-to-jet interaction that affects the spatial heat transfer distributions considerably. With certain flow conditions, the secondary heat/mass transfer maximum could develop in the interaction zone [12–16]. When the jet Reynolds number and separation distance are respectively large and small, a ring of the secondary stagnation-heat-transfer contour that surrounds the central confined jet appears [14]. The values of the secondary stagnation heat transfer rate could be sometimes comparable with the stagnant point level [12–16] and increase with the increase of Reynolds number but decrease with the increases of nozzle-to-nozzle spacing [2,17] and separation distance [14]. This experimental observation typifies an influence of the boundary layer transition on heat transfer owing to the radial flow acceleration and deceleration, which mechanism is affected by the jet-to-jet interaction and the resulting pressure field over the impinging surface. When the separation distance gradually increases, a transition of the central jet from the confined submerged flow to the free surface like jet-flow takes place due to the weakened jet-to-jet interaction. With the attempt to employ the impinging jet-array for the cooling of electronic device, the recent development of micro-instrument has become the prerequisite to use the impinging jet-array with very small separation distance (e.g., $S/D_j < 1$). Furthermore, as the integration density of each microelectronic circuit in a component such as CPU in computer or over the components in an IC board may be different, the cooling requirement for each electronic component under a jet-array varies spatially. In order to accommodate the various heat fluxes dissipated from different integrated circuits, the cooling effectiveness of each individual jet in an array could be accordingly adjusted by fitting nozzles with different diameters in an orifice plate. In the past, only few research efforts dealt with the array of impinging jets with very small separation distance ($S/D_j < 1$). None of the aforementioned works have studied the heat transfer of impinging jet-array issued from the grooved surface that is organized by nozzles with different diameters. To this end, the detailed heat transfer measurements for three jet arrays depicted in Fig. 2 are performed. The 3×3 jet-array (test module A) organized by nine equal-diameter nozzles, in which three jets in the central column are issued from a vertical groove, is initially treated to provide the baseline heat transfer data. With the smaller nozzles to replace the nozzles in the central column and side columns of the baseline array respectively, the test modules B and C are configured and tested. The detailed distributions of local Nusselt number contours and spatially averaged heat transfer data, evaluated from the infrared thermal images of the impinging surfaces, are presented over a range of separation distances and Reynolds numbers for all three test arrays. The impacts of grooved orifice plate and distributions of nozzle-size on heat transfer are subsequently analyzed to assist the derivation of empirical heat transfer correlations.

2. Experimental details

2.1. Apparatus

The experimental apparatus is shown in Fig. 2. The test fluid, pressurized air, was directed via a flow calming tube (1) with equivalent straight length of 300 mm into a settling chamber of dimensions $60 \times 60 \times 120$ mm (2), and ejected from the nozzles through the orifice plate (3). All the jet-arrays for test modules A, B and C were arranged in the in-line manner. The jet diameter, D_j, for the test module A remained at 5 mm; while the 3 mm nozzles replaced the 5 mm nozzles in the central column and side columns from the test module A that respectively configured the test modules B and C. A central 15×120 mm vertical rectangular groove with depth of 10 mm was machined on the surface of each orifice plate (3). Using the jet diameter of 5 mm as the characteristic length, the width, height and depth of the central vertical groove are respectively 3, 24 and 2 jet diameters. The thickness of orifice plate (3) was two jet diameters. Each nozzle had abrupt inlet and exit. The dimensionless jet-to-jet spacing, H/D_j, was 4 for all the test modules. Prior to entering the flow calming section (1), the air fed form the IWATA SC 175C screw-type compressor unit was dehumidified and cooled to the ambient temperature through a refrigerating unit that was integrated with the compressor. The dry and cooled airflow was then guided through a set of

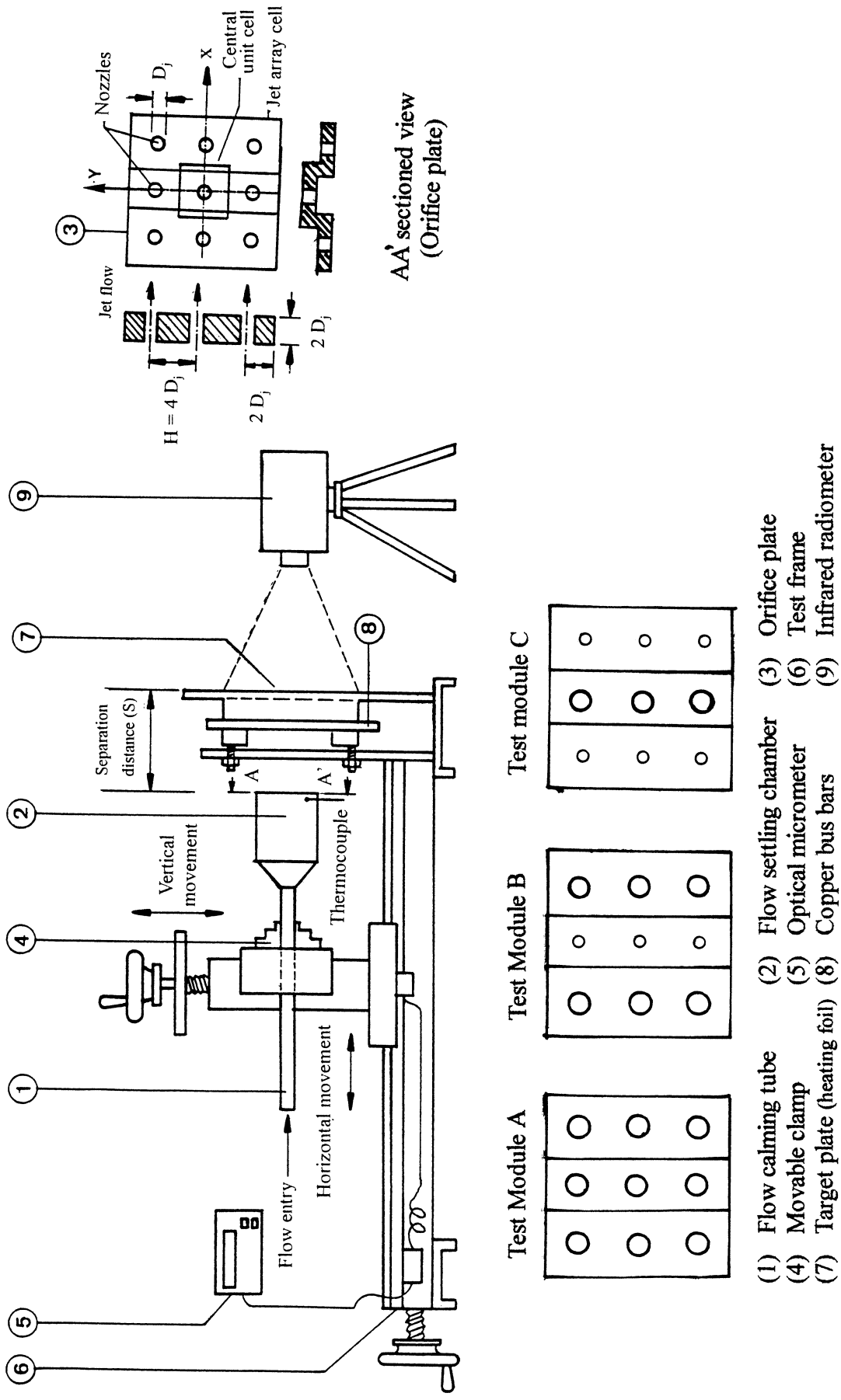

Fig. 2. Schematics of experimental apparatus and test modules.

pressure regulator and filter with the flow rate to be metered and adjusted by a Tokyo Keiso TF-1120 mass flow meter and a needle valve respectively. The complete jet-array unit was fixed and centered on a movable clamp (4). The vertical and horizontal movements of this clamp (4) were adjusted by two independent thread mechanisms, which could be precisely adjusted in order to center the jet-array and to control the separation distance. An optical micrometer (5) with the precision of 0.01 mm was mounted on the test frame (6) to measure the separation distance from the target plate (7). With the assistance of the precision provided by the optical micrometer, the tests with very small separation distance ($S/D_j < 1$) could be performed.

The jets issued from the orifice plate impinged horizontally against a very thin (0.1 mm) and 120 mm wide stainless steel foil (7). This heating foil (7) was stretched tightly between two copper bus bars (8). The adjustable high current DC electrical power was directly fed into the steel foil (7) to generate the basically uniform heat flux surface. The foil deflection and dimpling under the maximum Reynolds number tested at separation distance of 0.1 jet diameter was less than 0.02 mm as measured by a precision caliper. The temperatures of the heating surface under each test condition were imaged by a two-dimensional NEC TH3101-MR infrared radiometer (9). For this thermal image processing system, it took 0.3 seconds to complete a full-field of 239×255 matrix scan. The back surface of the heating foil (7) was painted flat black in order to minimize the background reflection and to increase the emission.

2.2. Program and procedures

The experimental program involved two phases. Initially the effect of grooved orifice plate on heat transfer was checked out with a series of baseline tests using the orifice plate fitted with equal-diameter nozzles (module A), over a range of separation distances and Reynolds numbers tested. This was followed by a similar series of experiments for test modules B and C. With the same ranges of flow and geometric parameters, the heat transfer results from the two phases were compared to reveal the heat transfer modifications caused by the different distributions of non-equal-diameter nozzles. The jet-array configuration which provided higher spatially averaged heat transfer rate under the condition with the same total flow consumption was disclosed through this comparative analysis. Finally, the empirical correlations for the spatially averaged heat transfer rates over the entire and central-jet areas of the three jet-arrays were derived as the strategic aim of the present study.

For each individual test, the apparatus was allowed to achieve steady state. A steady state was assured when the variations of wall temperatures over the impinging surface were less than 0.2 °C for each test at the predefined flow rate and heating power. It generally took about 25 minutes to reach the steady state when the variation of flow rate, heating power or the separation distance was made. The on-line infrared thermal-image data capture system was then activated to record the full field wall temperature distributions over the impinging surface. Along with the measured heating power and jet temperature, T_j, the local Nusselt number distributions at the prescribed Reynolds number and separation distance were evaluated. With tests at each $Re - S/D_j$ options, the heater powers were adjusted to maintain the central stagnant wall temperatures at 45 °C. This is aimed at remaining the buoyancy at the approximately same level for all the tests performed so that the buoyancy interaction could be isolated from the present investigation. To verify this attempt, the local Grashof numbers were evaluated as a convenient account for the relative strength of buoyancy. The local value of density ratio, $\Delta\rho/\rho$, involved in the Grashof number was determined as $\beta(T_w - T_f)$ following the Boussinesq's approximation. The β value was evaluated as $1/T_f$ for perfect gas with the local film temperature, T_f, to be defined as the averaged value of jet and local wall temperatures. Note that, although the spatially averaged Grashof numbers over the entire heating area for all the tests were controlled in the range of 577–618, it is still infeasible to control the entire full-field wall temperatures at the exactly same values owing to the variations of flow field caused by varying the flow parameters. Table 1 summarizes the range of the non-dimensional parameters investigated for all the test modules.

It is worth noting that, when the jet array is issued from the orifice plate, the pressure distribution over the impinging surface varies with the flow and geometric parameters such as Reynolds number, separation distance and the predefined confinement. As a result, the rate of mass flow through each nozzle in the orifice plate is different and is functionally related with Re, S/D_j and geometric features of the jet-array system [10]. The adjustment of Reynolds number or the geometric parameters in the jet-array system provides a unique mass flux distribution for the jets issued from the orifice plate. The different mass flow rate through each nozzle in an array issued from the orifice plate reflects the realistic flow phenomena when the jet arrays are issued from an orifice plate during the engineering application, which effects on heat transfer have also been an engineering focus for investigation [10–13]. The present experimental study adopts the parametric approach to characterize the heat transfer of impinging jet arrays issued from the orifice plates using the controlling dimensionless flow and geometric parameters. When the flow and geometrical features, such as the Reynolds number, the jet-array configuration and the separation distance are selected, the flow field over the impinging surface is generated and the influences of varying the total mass flow rate, separation distance and the configuration of jet-array on heat transfer are systematically

Table 1
Range of experimental parameters investigated

Jet Reynolds number (Re)	1000, 1500, 2000, 3000, 4000
Grashof number range (Gr)	577–618
Separation distances (S/D_j)	0.1, 0.25, 0.5, 1.0, 1.5, 2, 2.5, 3, 4, 6, 8

investigated. The present study attempted to compare the various heat transfer performances of test modules A, B and C under the same amount of total coolant consumption. Thus the characteristic length selected to define the Nusselt; jet-Reynolds and Grashof numbers was unified as the jet-diameter of baseline array, D_j, with the Reynolds number to be specified as $\frac{4}{9\pi}\frac{\dot{M}}{D_j\mu}$; even if the 3 mm and 5 mm orifices configured the test arrays B and C. The range of Reynolds numbers tested ensured the laminar, transitional and turbulent jets were examined because the jet became turbulent with $Re \geqslant 3000$ [18]. However, even though the jets were laminar at the nozzle exits, there was possibility for them to become turbulent when the jets deflected upon impingement and developed as the wall-jet flows.

To evaluate local Nusselt number, the convective heat flux, q, was calculated from the electrical dissipation measured over the entire heating surface with the heat loss to be subtracted. The characteristics of external heat loss at different heating levels were determined through a number of heat loss calibration runs. For each set of calibration runs, the flow was blocked off and the impinging surface was fitted with thermal insulation. Under such circumstance, the heat supplied to the heating foil was entirely lost into atmosphere from the back of the impinging surface and balanced with the amount of heat loss at the corresponding steady-state temperature distribution. As the electrical heating power and the thermal insulation foils were uniformly applied, the distributions of wall temperature over the entire scanning area were uniform during each heat loss calibration run. A review of the temperature data collected from the calibration test runs showed less than 2.36% of non-uniformity in the wall temperature distributions. Thus, by plotting the heat flux applied for each heat loss calibration test against the corresponding steady wall-to-ambient temperature difference reveals the functional relationship between the heat loss flux and the prevailing wall-to-ambient temperature difference. It was found that the amount of heat loss increased with the local prevailing temperature difference between wall and ambient. The equation correlated from the heat loss experiments, which calculate the heat loss flux using the measured local wall-to-ambient temperature difference, was incorporated into the data processing program to evaluate the local heat flux convected by the flow. The jet temperature, T_j, was measured using a thermocouple penetrated into the plenum chamber as indicated in Fig. 2. The local Nusselt number is evaluated as

$$Nu = \frac{q\,D_j}{k_f(T_w - T_j)} \tag{1}$$

For the evaluation of jet Reynolds number, the coolant viscosity was determined from the jet temperature. The local fluid properties quantifying the local Nusselt and Grashof numbers were evaluated based on the local film temperature, T_f.

The experimental repeatability of temperature measurement using NEC TH3101-MR infrared radiometer was carried out for the baseline experiment. The maximum variations of wall temperature measurements with the flows to reach the same steady state conditions were in the range of $\pm 0.7\,^{\circ}\mathrm{C}$ for the present system. Thus the maximum uncertainty of temperature measurement was estimated as $\pm 0.7\,^{\circ}\mathrm{C}$, which became the major source to attribute the uncertainties for the coolant's thermal conductivity, fluid density and viscosity. Following the policy of ASME on reporting the uncertainties in experimental measurements and results [19], the maximum uncertainty associated with the local Nusselt, Reynolds and Grashof numbers were estimated to be 9.9, 5.5 and 7.6%, respectively.

3. Results and discussion

3.1. Groove effects

The heat transfer improvement for the most constrained jets in a large impinging jet-array with very small separation distances ($S/D_j < 1$) is attempted by introducing the additional space for the transportation of spent fluids from the inter-jet region using the vertical groove on the orifice plate. In this respect with very small separation distance, it is felt that the central-column jets upon the impingement on the target plate could be deflected into the groove that enriches the central-jet momentum through the enhanced entrainment. This mechanism could assist the heat transportation over the most constrained jet region in addition to the impact of favorable treatment of spent fluids when jets were issued from a groove. Also worth noting that, since the three jets in the central column of array are allocated in the groove as depicted in Fig. 2, the actual separation distance for these three jets increases $2D_j$. This groove also modifies the pressure field and wall-jet flows over the impinging surface, under which the wall-jet flow is three-dimensional. It is therefore the combined groove-induced effects and the influences of different distributions of nozzle size on heat transfer that the present study focuses. Prior to the detailed evaluation for the impacts of distributions of nozzle-size on heat transfer; the general groove-induced effects are illustrated. To highlight these impacts, two sets of comparable results obtained from the smooth-walled [20] and grooved orifice plates (module A) with the same values of Re and S/D_j are depicted in Fig. 3.

Fig. 3(a) shows the distributions of Nusselt number contour at $4S/D_j$ over the entire scanned area with jets issued from the smooth-walled and grooved orifice plates, in which the boundaries of central unit cell and impinging jet array along with the flow paths of radial spent fluids are specified. As shown, the Nusselt number contours with the jet-array issued from smooth-walled orifice plate at $4S/D_j$ are quite symmetrical. This observation reveals the free surface like jet-flow in the central jet region due to the weakened jet-to-jet interaction so that the stagnant Nusselt number for each jet in the array issued from the smooth-walled orifice plate is

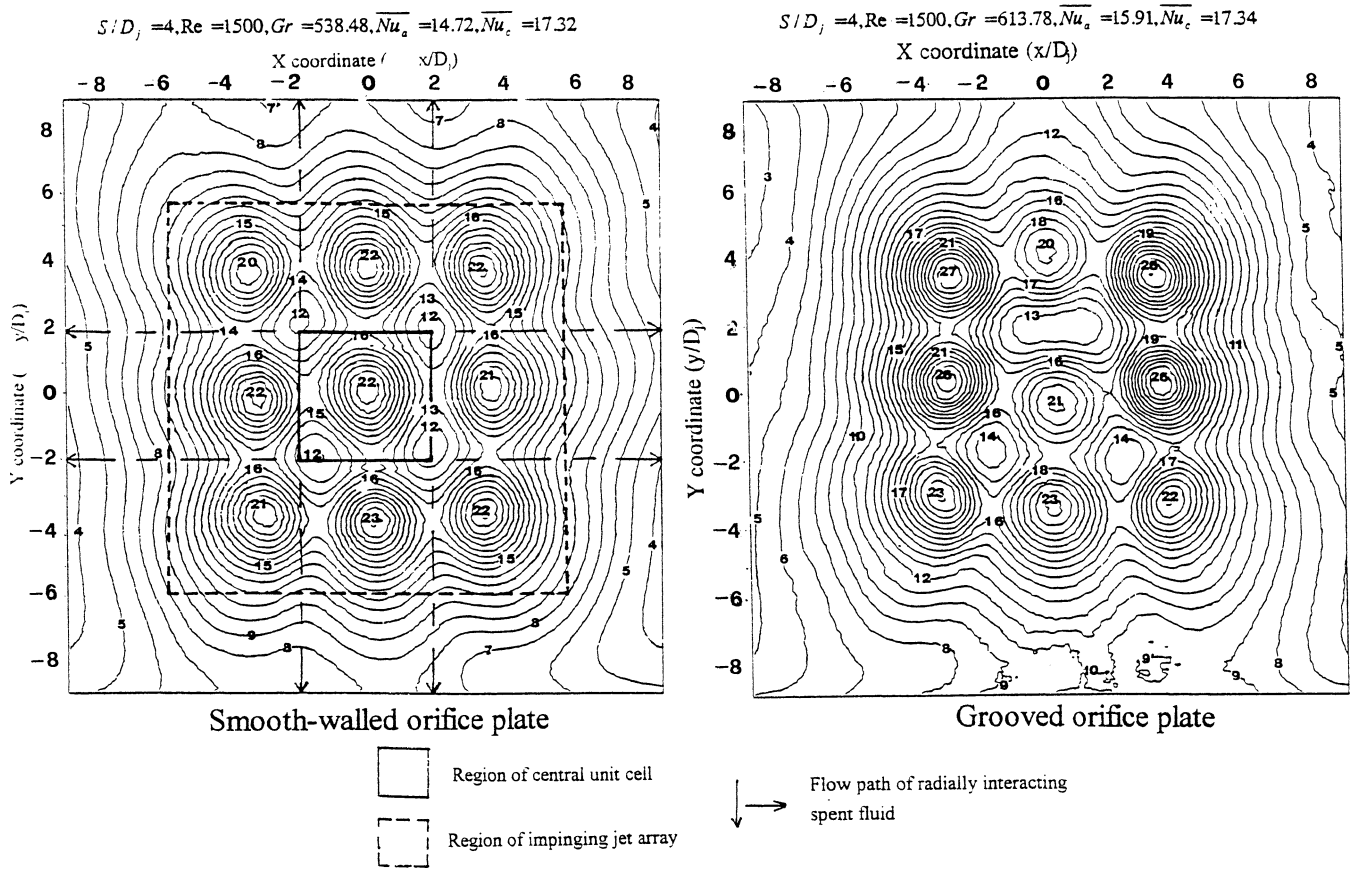

(a)

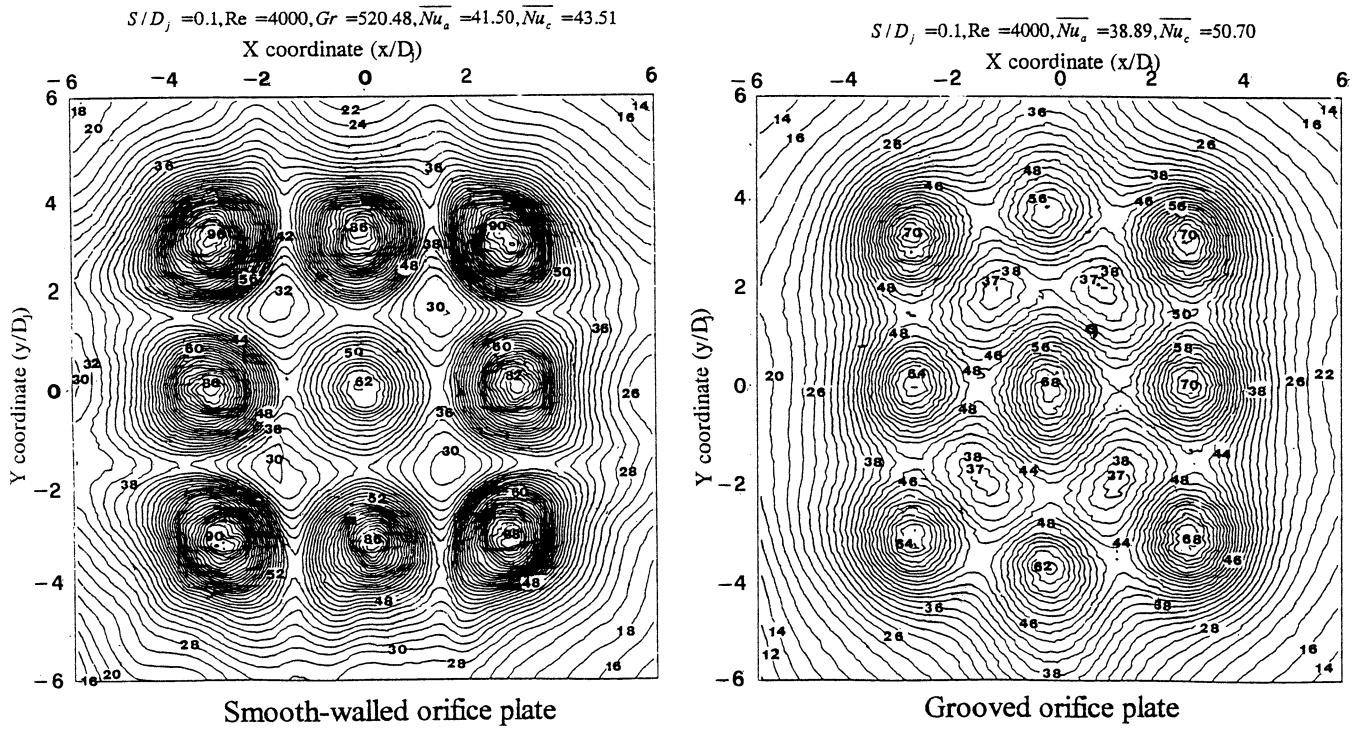

(b)

Fig. 3. Distributions of Nusselt number contour over impinging surface with jets issued from smooth-walled and grooved orifice plates: (a) Typical results with $S/D_j > 3$. (b) Typical results with small separation distance ($S/D_j < 1$).

similar. A cross examination of heat transfer results for the two scenarios depicted in Fig. 3(a) shows that the stagnant and spatially averaged Nusselt numbers over the central jet regions for the two comparable cases are similar but the heat transfer distributions are different. A detailed illustration in this regard has been previously reported [20]. However, it is worth noting that there are regions of concave Nusselt number surfaces developed at the inter-jet regions. The locally minimum Nusselt numbers in these regions generally take place at the intersections of the flow paths along which the radial spent fluids are convected. This heat transfer impediment reflects the influences of weakened wall-jet flow momentum and thickened boundary layers due to the collision of radial spreading flows. With grooved orifice plate, the top and bottom jets in the groove are shifted radially outward with considerable jet enrichment found for the top two corner jets; and there could be three or four areas with concave Nusselt number surfaces in the inter-jet regions as typified in Fig. 3(a) and (b). The offset of stagnant point for the top and bottom jets in the groove is apparent especially when the separation distance is small, which reflects an impact of strong crossflow in the groove. Unlike the smooth-walled orifice plate, the patterns of heat transfer distribution are sensitive to the separation distance when the jets eject from the grooved orifice plate. This phenomenon will be examined in more details when the baseline results are illustrated. Having defined the boundary of jet-array region in Fig. 3(a), only the detailed heat transfer measurements over the region of impinging jet area will be presented in what follows. With $0.1S/D_j$ as shown in Fig. 3(b) for the smooth-walled orifice plate, the stagnant Nusselt number value of central jet is considerably lower than the stagnant value of its surrounding jet. The central jet-flow is significantly confined by the surrounding jets and becomes submerged flow at very small separation distance. At the separation distance of $0.1S/D_j$, the jets around the central jet issued from the smooth-walled orifice plate underwent considerable enrichment, which led to the considerable confinements for the central jet. As a result, the stagnant Nusselt numbers for the jets around the central jet of smooth-walled orifice plate are much higher than the central jet value. When the jets in the central column of array eject from the vertical groove at $0.1S/D_j$ as shown in Fig. 3(b), the stagnant heat transfer level of central jet becomes comparable with its surrounding jet values in the grooved orifice plate. This result indicates the less amount of jet enrichment for the surrounding jets in the grooved orifice plate relative to the scenarios observed for the smooth-walled orifice plate, which reflects a groove effect that assists the removal of spent fluid in the central jet region. As compared in Fig. 3(b), the groove-induced effects cause about 15% of heat transfer increment over the value obtained with the smooth-walled orifice plate at the stagnant point of central jet. The improved heat transfer performance provided by the groove at the small separation distance is demonstrated.

3.2. Impacts of different distributions of nozzle sizes in grooved orifice plate

The heat transfer impacts of different distributions of nozzle sizes in the grooved orifice plate are examined by comparing the results between test modules A, B and C obtained with identical values of *Re* and S/D_j. Figs. 4, 5 and 6, respectively, show the distributions of Nusselt number contour with various values of *Re* and S/D_j over the impinging surfaces for test modules A, B and C. Each graph shown in Figs. 4–6 is plotted with a constant interval between the Nusselt number contours. This manner of presentation enables the direct comparison between the results summarized in Figs. 4–6. The relatively dense Nusselt number contours in any controlled area reflect the higher gradients of spatial heat transfer variations. Also worth noting that, the systematic increase of S/D_j or *Re* at a fixed value of *Re* or S/D_j depicts the isolated effect of S/D_j or *Re* on heat transfer. These isolated S/D_j or *Re* effects are revealed when the plots along each column or row of Figs. 4–6 are compared, respectively.

Although the orifices have the same diameter in jet-array A, the individual jet entrainment and confinement, the crossflow and the surface pressure distributions over the impinging surface are altered due to the influences of groove. Owing to the presence of groove, the jet-to-jet interactions vary spatially and are affected by S/D_j and *Re* in some ways. The heat transfer distributions around the nine stagnant points are no longer symmetrical about the center of jet-array and vary with S/D_j as demonstrated in Fig. 4. As shown, the stagnant Nusselt number values in the central column of array are reduced from the jets in the adjacent columns when $S/D_j > 1$. Such relative low heat transfer rate in the central column region implies that there is no appreciable jet enrichment for the central column jets due to the groove effect when $S/D_j > 1$. Instead, the confinements provided by the jets of side columns reduce the heat transfer over the central-column region. Led by an examination of all versions of Fig. 4 with $S/D_j > 1$, it is found that the stagnant Nusselt numbers for the upper, middle and lower jets in the central column of array generally correspond to the minimum, medium and maximum values respectively; since the stronger crossflow develops in the upper region of the groove due to the upward buoyant flow which deteriorates the local heat transfer further. But with small separation distances ($S/D_j < 1$) as shown in Fig. 4, the middle jet in the central column turns into an effective cooling element in the array. Apparently, the jet momentum of this central jet is enriched when $S/D_j < 1$. It is thus expected that the deflected central jet upon impingement on the target plate is confined by the surrounding jets to roll up in the groove, which effect enhances the entrainment of central jet and leads to its jet-enrichment. Such mechanism, which leads to heat transfer enhancement for the central jet, shall likewise occur in a larger array system that formulates

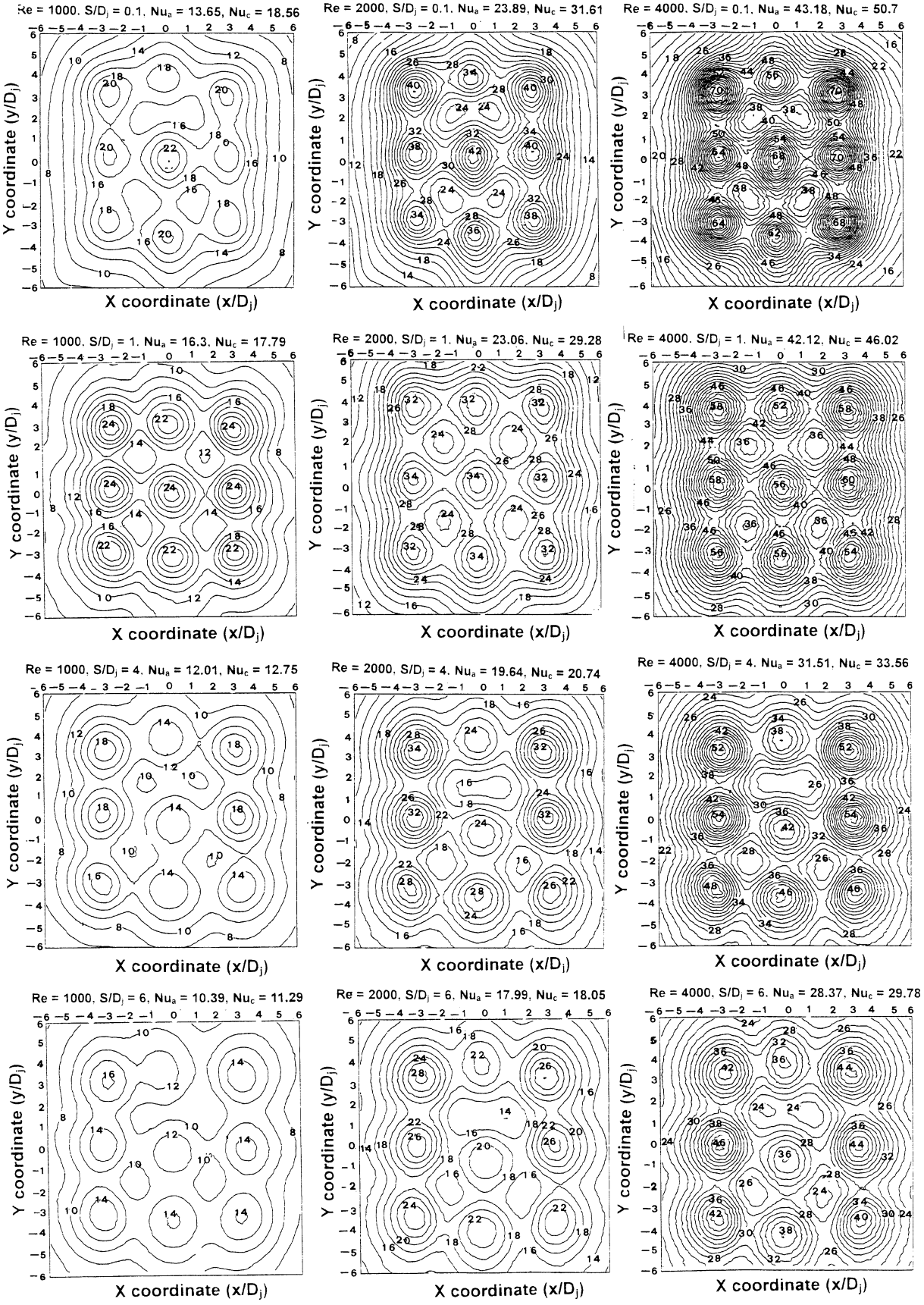

Fig. 4. Distributions of Nusselt number counter over the impinging surface of test module A.

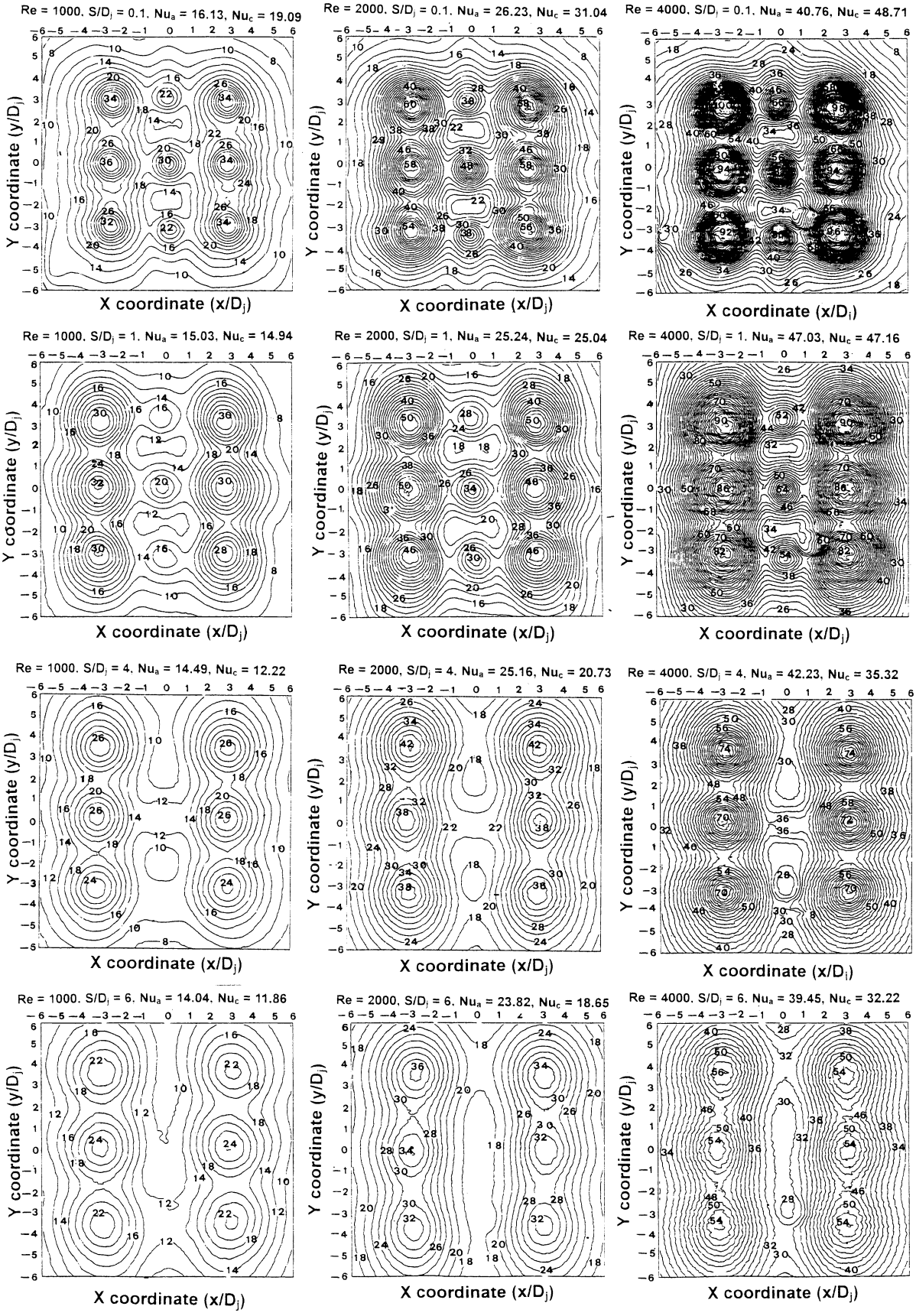

Fig. 5. Distributions of Nusselt number counter over the impinging surface of test module B.

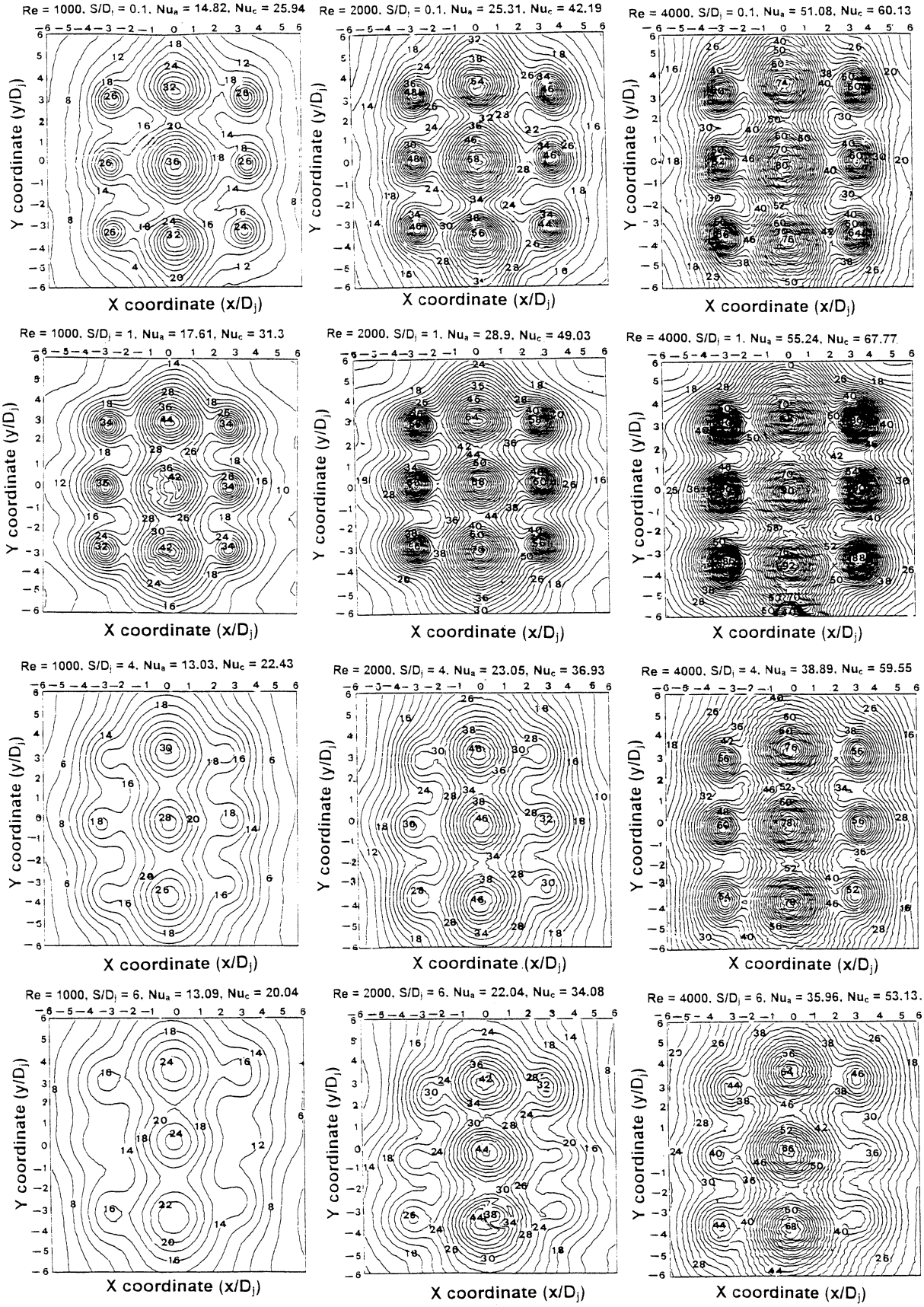

Fig. 6. Distributions of Nusselt number counter over the impinging surface of test module C.

the basis for heat transfer augmentation using the grooved orifice plate when the separation distances are very small.

When S/D_j increases from 0.1 at a selected *Re* value as displayed in Fig. 4, the most considerable heat transfer variations take place in the central-column region. As shown when S/D_j increases, the heat transfer levels and the effective cooling areas in the central-column region are gradually reduced. The top two concave Nusselt number surfaces found at $1S/D_j$ merge into one region when S/D_j increases further. Accompanying with this variation is the gradually faded jet-offset phenomenon found in the central column of array. The values of spatially averaged Nusselt numbers, Nu_a and Nu_c, generally decrease against S/D_j. At any fixed separation distance, the increase of jet Reynolds number increases the levels and gradients of Nusselt number contours. Unlike the effects caused by varying S/D_j, the characteristic features of Nusselt number distributions are not significantly modified when *Re* increases although the increase of Reynolds number from 1 000 to 4 000 transits the jets from laminar to turbulent flows.

With the central column jets to be issued from the smaller orifices, the effective cooling areas over the regions of central and side columns are, respectively, suppressed and enhanced when the test results in Figs. 5 (module B) and 4 (module A) are compared. The effective cooling areas for the central-column jets of test array B are squeezed down by the stronger confinements provided by their adjacent jets. Within the range of separation distances examined, the stagnant Nusselt numbers in the side columns of jet-array B are consistently higher than their counterparts in the jet-array A due to the less confinements or/and the jet-enrichments attributed from the central-column jets. The stagnant Nusselt number values in the side columns of jet-array B increase about 30% over the corresponding values in the baseline array. At $0.1S/D_j$ as shown in Fig. 5, the values and gradients of Nusselt number contours over the central column region are less than those of side-column regions. Nevertheless, by comparing the test results found at 0.1 and $1S/D_j$ as depicted in Fig. 5, it reveals that the stagnant and gradient of Nusselt numbers over the central column region are increased at $0.1S/D_j$, which indicates the presence of groove effect. Relative to the results found at $0.1S/D_j$ with jet-array A, it is interesting to note that the values and gradients of Nusselt number contours over the effective areas of central-column jets for test module B are also increased. However, instead of four closed-looped heat transfer impeding regions developed midways between the jets as shown in Fig. 4, there are only two close-looped concave Nusselt number surfaces found in the central column of jet-array B when $S/D_j = 0.1$. The spatially minimum Nusselt numbers in these impeding loops shown in Fig. 5 are less than the corresponding values in Fig. 4. These observations suggest that the enhanced jet enrichment over the grooved region at very small separation distances ($S/D_j < 1$) is accompanied by the stronger inter-jet confinements when the sizes of orifices in the groove are relatively small. With $S/D_j \geqslant 4$, the jet identities, typified by the circular close-lopped Nusselt number contours, eventually disappear form the central column region. Beyond this separation distance ($4S/D_j$), the heat transfer contours in the central column region gradually merge into the jointed oval loops when both values of S/D_j and *Re* increase. At $6S/D_j$, the Nusselt number surface over the central column region becomes rather flat. Therefore the mass fluxes issued from the central column jets could not directly impinge on the target plate but are totally entrained to enrich the side-column jets when the separation distance increases above $4S/D_j$ that is about the length of potential core for a side-column jet. Justified by the enhanced cooling effectiveness of side-column jet in test array B over the range of separation distances tested, there are certain amounts of mass flux from the central-column jets being entrained into the side-column jets before the jets hit the target plate. In view of the increased effective areas for the side-column jets with the increased S/D_j value, the dependency of jet-entrainments for the side-column jets on S/D_j is demonstrated. Such dependency could also be affected by the different radial spreading rates of jets when the nozzle sizes in an array vary. This leads to the coupling effects between *Re* and S/D_j, which will be further examined when the isolated S/D_j and *Re* effects are illustrated. To this end, the above experimentally based observations suggest that the distributing patterns and values of Nusselt number contours are very sensitive to the variation of S/D_j for a jets-array organized by the nozzles with different sizes. However, similar to the phenomena found with baseline jet-array, the patterns of Nusselt number distributions are not significantly modified by Reynolds number. The inter-jet reactions or the patterns of radial momentum distribution over the impinging surface of test array B are therefore the strong and weak functions of S/D_j and *Re*, respectively.

The array configuration made by replacing the smaller orifices from the side columns of baseline array turns the central-column jets into the very effective cooling elements as demonstrated in Fig. 6. It is apparent that the jets issued from the central vertical groove undergo very considerable enrichments. As a result, the Nu_c values of test module C are considerably increased from the levels found in test modules A and B. The central-column jets always remain as the most effective cooling elements in test module C for all the S/D_j values examined. For this test array, the features of Nusselt number distributions are not altered by the increase of S/D_j at any fixed Reynolds number. Nevertheless, unlike the results found in jet-arrays A and B, the values of Nu_c at $0.1S/D_j$ for all the Reynolds numbers tested are consistently lower than the results obtained with $1S/D_j$ as typified in Fig. 6. Led by an examination of all the data generated with test module C, the maximum Nu_c for each specified Reynolds number appears at $0.5S/D_j$. With relatively small values of *Re* and large separation distances, such as the results depicted in Fig. 6(c), (d) and (h), the identities of side-column jets become vague. With these scenarios, the mass fluxes

issued from the side-column jets are partially entrained into the central-column jets. Therefore the enhanced cooling effectiveness over the central-column region in test array C is caused by the combined effects of groove and the additional jet enrichment attributed from the side-column jet. Depending on the values of *Re* and S/D_j, the increments of stagnant Nusselt numbers for the central-column jets of test array C reach about 50–95% of the baseline levels. The arrangement of jets with the larger size in the groove appears to be an effective measure for local heat transfer augmentation. Another feature worth noting in Fig. 6 is the disappearance of the close-looped concave Nusselt number surfaces developed midways between the adjacent jets. This phenomenon is consistently observed that reflects the improved transportation of spent fluids from the inter-jet regions of jet-array C. Although the mass fluxes of side-column jets could be partially entrained into central-column jets, the stagnant Nusselt numbers of side-column jets found in Fig. 6(a), (b), (e), (f), (i), (j) and (h) are still higher than the baseline levels. In this respect, the range of separation distances, over which the heat transfer rates in the side-column regions of test module C are higher than the baseline results, increases with the increase of *Re*. But the patterns of Nusselt number distributions showed in Fig. 6 are not significantly modified by *Re* or S/D_j for test array C.

3.3. Isolated S/D_j and Re effects

A variety of heat transfer distributions over the impinging surfaces of test modules A–C have been revealed in Figs. 4–6. These results reflect the combined effects of groove and nozzle-size distributions with various S/D_j and *Re* values. The mechanisms, through which the variations of S/D_j or/and *Re* modify the heat transfers, involve the groove effects; the gain or loss of mass flux for the individual jet in an array; and the modified inter-jet reactions that varies the distributions of wall-jet flows. Because these mechanisms are inter-related with S/D_j and *Re*, the coupling S/D_j–*Re* effects are identified, especially when the orifices with different diameters organize the jet-array. To illustrate the isolated effect of S/D_j on spatially averaged heat transfer, two sets of examples that compare the variations of Nu_a and Nu_c against S/D_j at fixed *Re* between test modules A, B and C are shown in Figs. 7 and 8. Through this comparison, the favorable test module with the optimal S/D_j value that results in the highest value of Nu_a or Nu_c at a selected Reynolds number are identified. As shown in Fig. 7(a) and (b) with $S/D_j > 3$, B array poses the highest Nu_a values. With $S/D_j < 2$, the module C provides the highest values of Nu_a for both Reynolds numbers examined, except at $0.1S/D_j$ as plotted in Fig. 7(a). The S/D_j value for each test array that corresponds to a spatially averaged peak value of Nu_a in Fig. 7(a) appears at 0.25, 0.1 and 0.5 for test modules A, B and C, respectively. When *Re* increases to 4 000 as shown in Fig. 7(b), the larger values of Nu_a occur at 0.1, 2 and $0.5S/D_j$ for test modules A, B and C. The

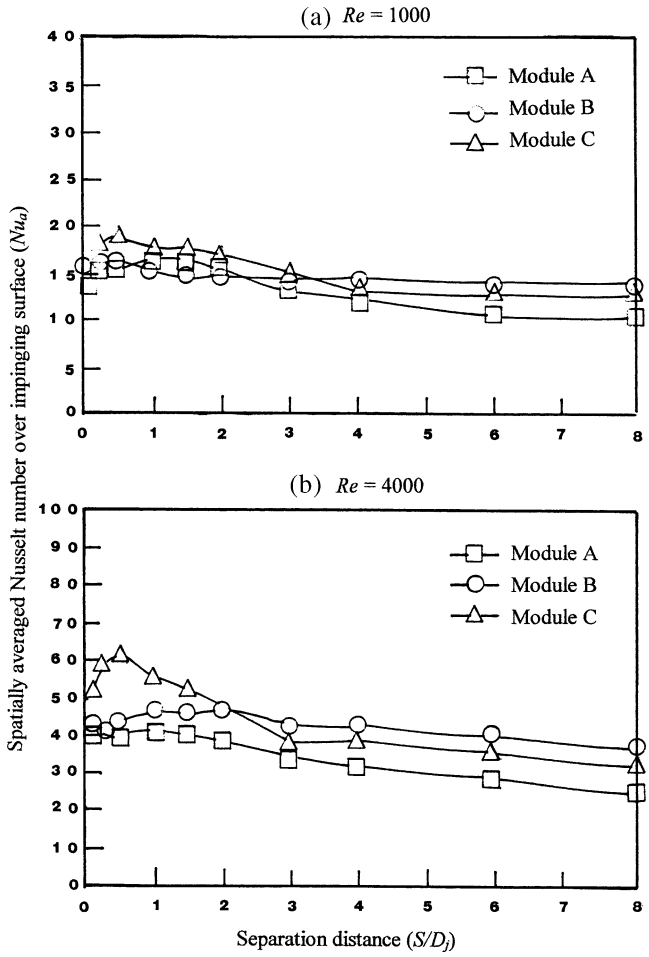

Fig. 7. Variations of spatially averaged Nusselt number over impinging surfaces of test modules A, B, and C.

S/D_j value at which the higher Nu_a is produced becomes Reynolds number dependent due to the interactive S/D_j–*Re* effects. Thus the optimal selection of S/D_j value varies with *Re* for each tested array. In Fig. 7, it apparently depicts that Nu_a of test module C initially increases to a peak value when S/D_j gradually increases from 0.1. After passing this peak value, a monotonic decrease of Nu_a with increase of S/D_j is followed. With respect to the Nu_c–S/D_j relationship, the variation patterns of test module C depicted in Fig. 8(a) and (b) are similar with the results revealed in Fig. 7(a) and (b); but the S/D_j value that corresponds to a spatially averaged peak value of Nu_c takes place at 0.5. Among the array configurations tested, the jet-array C consistently offers the higher values of Nu_c in the range of S/D_j values examined. The obvious local heat transfer enhancement in Nu_c by fitting the larger orifices in the grooved central column of array is demonstrated. The Nu_c values for test modules A and B generally decrease with the increase of S/D_j as illustrated in Fig. 8, which leads to the largest Nu_c values developed at $0.1S/D_j$. Led by an examination of all versions of Figs. 7 and 8 for all the Reynolds number tested, it concludes that C array generally offers higher heat transfer rates for both Nu_a and Nu_c at small separation distances ($S/D_j < 2$). Recall

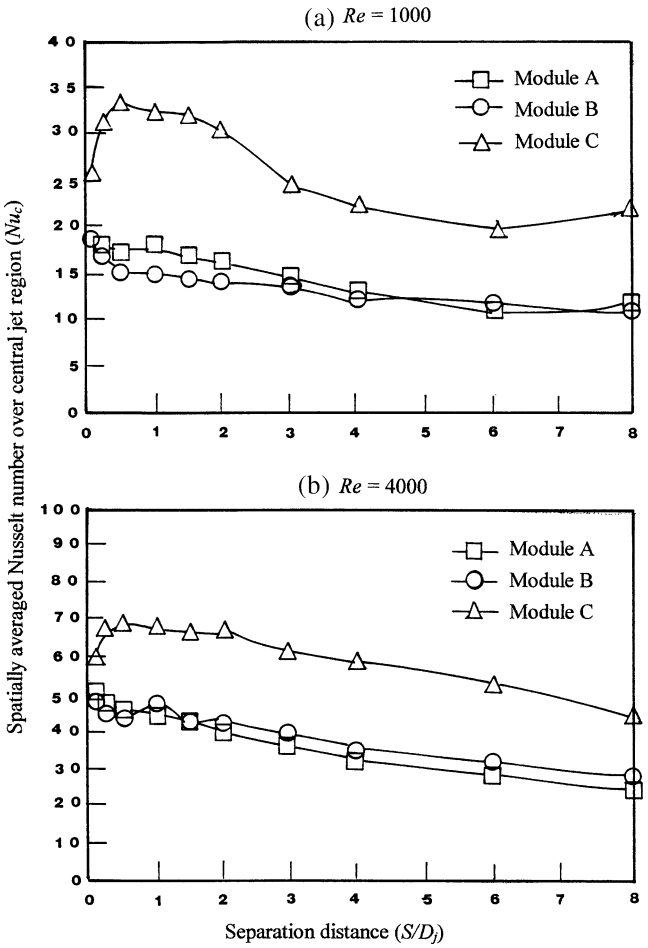

Fig. 8. Variations of spatially averaged Nusselt number over central jet regions of test modules A, B, and C.

the results depicted in Fig. 6, the concave Nusselt number surfaces observed in the midways between the adjacent jets of test modules A and B are vanished in the contour plots of C array. This phenomenon implies the more efficient transportation of spent fluids from the inter-jet regions in jet-array C. As a result, the higher values of Nu_a with $S/D_j < 2$ for test module C are observed in Fig. 7. Therefore the orifices with larger diameters shall be fitted in the groove of orifice plate in order to gain the higher local and overall heat transfer rates at the small separation distances.

The isolated *Re* effects are examined by plotting the Nu_a and Nu_c against *Re* at fixed S/D_j for each test array. Fig. 9 displays the *Nu–Re* relationship at a number of S/D_j values for jet-arrays A, B and C. As shown, depending on the array configuration and the value of S/D_j examined, Nu_a and Nu_c increase with *Re* at different increasing rates. For test array A (see Fig. 9(a)), the Nu_a and Nu_c curves in each individual plot are quite parallel. Therefore the Nu_a and Nu_c follow the similar Reynolds number dependency at a fixed separation distance for A array. The value of Nu_c for jet-array A at each Re–S/D_j option is consistently higher than the Nu_a due to the groove effects. When the *Nu–Re* relationships for test array B are examined and compared with test array A, it is obvious that the increasing rates of Nu_a and Nu_c in each individual plot shown in Fig. 9(b) become different and vary with S/D_j. At each Re–S/D_j option, the different increasing rates between Nu_a and Nu_c curves suggest the differently regional Reynolds number dependencies. This heat transfer feature reflects the combined impacts provided by the central vertical groove and the distributions of nozzle size. As compared in Fig. 9(b) for the results with different S/D_j values, the different increasing rates for Nu_a or Nu_c curves reflect that the *Nu–Re* relationships for test array B are functionally related with S/D_j. At this stage, the existence of coupling Re–S/D_j impacts on the spatially averaged heat transfer for B array is highlighted. The effects of Reynolds number or separation distance on heat transfer are mutually influenced. Due to the coupling Re–S/D_j effects, the values of Nu_c are higher than Nu_a with $S/D_j < 1.5$. Further increase of S/D_j value for B array yields the relationship of $Nu_c > Nu_a$ to $Nu_c < Nu_a$ when $S/D_j > 1.5$. Note that, in view of the contour plots collected in Fig. 5, the central column jets start losing their identities when $S/D_j \geqslant 2$. Due to the weakened momentum for central-column jet and the moderated groove effect in B array when S/D_j increases above 2, the relationship of $Nu_c < Nu_a$ stands. For test array C, the different *Re* dependencies between Nu_a and Nu_c at each fixed separation distance still prevail as demonstrated in Fig. 9(c) owing to the impacts provide by the distribution of non-equal-diameter nozzles in the array. Justified by the various increasing rates of Nu_a or Nu_c with *Re* at different values of S/D_j shown in Fig. 9(c), the *Nu–Re* relationship for C array is still affected by S/D_j due to the Re–S/D_j coupling effects. However, as the central column jets always remain as the most dominant cooling elements in C array, the result of $Nu_c > Nu_a$ consistently holds over the entire range of separation distances tested.

3.4. Empirical heat transfer correlations

The derivation of empirical heat transfer correlations to evaluate the spatially averaged Nusselt numbers, Nu_a and Nu_c, has to consider the individual and coupling S/D_j and *Re* effects. Led by the observation of all S/D_j versions of Fig. 9, in which the coupling S/D_j–*Re* impacts are consistently found to be present with test arrays, it is proposed that the empirical correlation could take the specific form of

$$Nu_{a,c} = \Phi_1 Re^{\Phi_2} \tag{2}$$

where Φ_1 and Φ_2 are functions of S/D_j. These equation structures are applied to the three test jet-arrays but with different Φ-functions. Note that, as the variations of S/D_j or/and *Re* induce very complex flow phenomena involving the modifications of groove effect, jet entrainment, and inter-jet reactions, the regression-type analysis using Eq. (2) reveals the curly versions of Φ-functions. In order to capture the variation patterns of Φ-functions against S/D_j in the range of separation distance $0.1 \leqslant S/D_j \leqslant 8$, the fourth

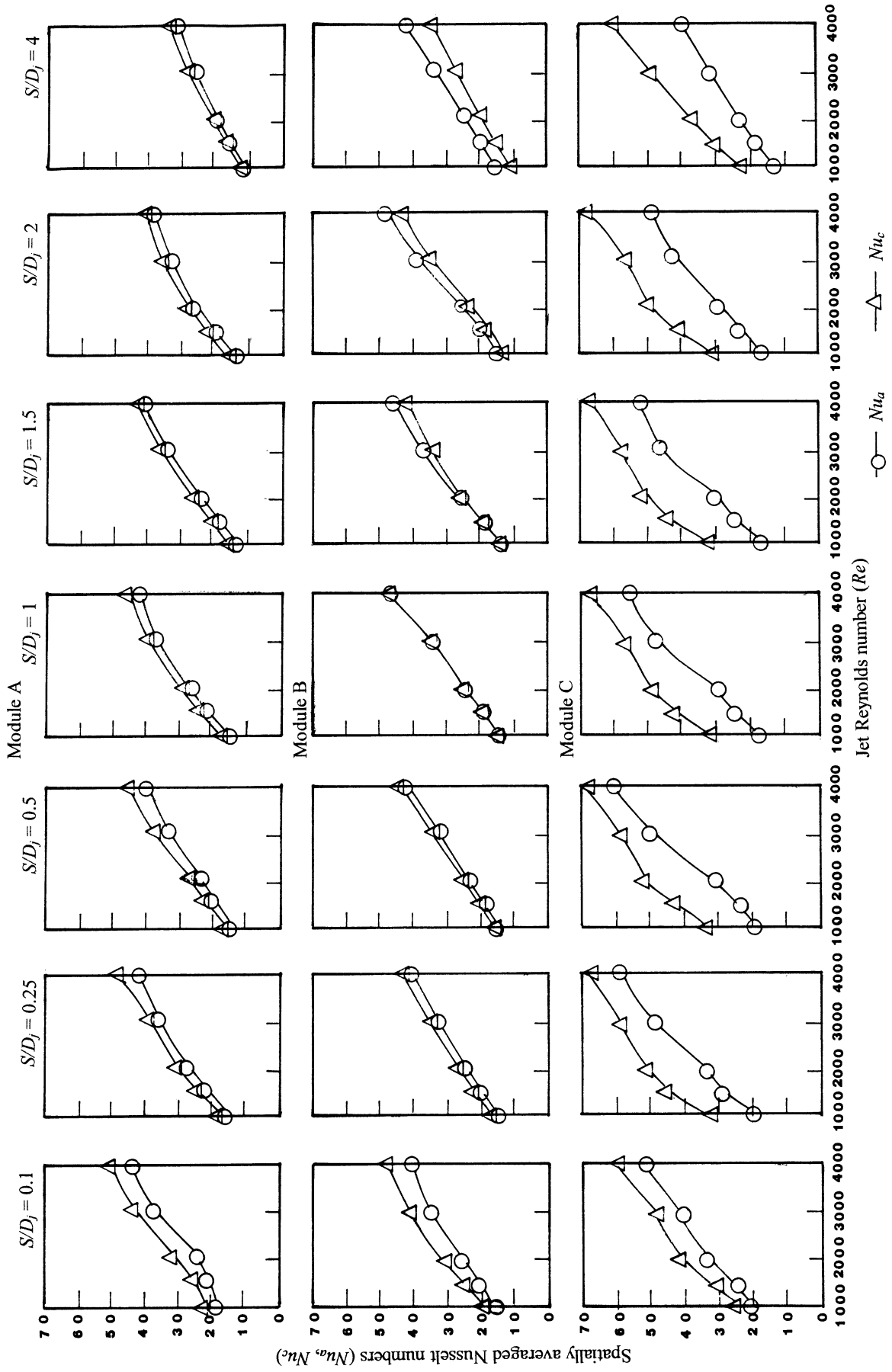

Fig. 9. Isolated *Re* effects on spatially averaged heat transfer.

Table 2
Coefficients of M_0–M_4 for test module A

	M_0	M_1	M_2	M_3	M_4
			Nu_a		
Φ_1	0.168	−0.0168	0.00462	−0.00177	0.000176
Φ_2	0.666	0.0233	−0.0158	0.00412	−0.000325
			Nu_c		
Φ_1	0.211	−0.054	0.0158	−0.00323	0.000255
Φ_2	0.657	0.0342	−0.0176	0.00411	−0.000321

Table 3
Coefficients of M_0–M_4 for test module B

	M_0	M_1	M_2	M_3	M_4
			Nu_a		
Φ_1	0.177	−0.210	0.0972	−0.0159	0.000855
Φ_2	0.632	0.337	−0.161	0.0264	−0.00143
			Nu_c		
Φ_1	0.197	−0.234	0.107	−0.018	0.001
Φ_2	0.64	0.309	−0.148	0.0248	−0.00138

Table 4
Coefficients of M_0–M_4 for test module C

	M_0	M_1	M_2	M_3	M_4
			Nu_a		
Φ_1	0.193	−0.275	0.163	−0.0319	0.00199
Φ_2	0.709	0.293	−0.194	0.0386	−0.0024
			Nu_c		
Φ_1	0.349	0.822	−0.481	0.0846	−0.00463
Φ_2	0.624	−0.173	0.103	−0.0176	0.000914

order polynomials for the Φ-functions have been adopted in the subsequently analysis. Each of the Φ-functions is assumed to take the general structure

$$\Phi_i = \sum_{j=0}^{j=4} M_j (S/D_j)^j \tag{3}$$

where the M_j are evaluated from the regression analysis applied to each Φ-function for a given jet configuration. Tables 2, 3 and 4 list the numerically determined curve fits for the M_j-coefficients for each of the Φ-functions for the test modules A, B and C, respectively. Fig. 10 compares the polynomial curve fits with the Φ-function values obtained from the data generated cross plots. As shown, the patterns of variations in Φ-functions against S/D_j are similar for all the jet-arrays tested. There appear different degrees of ripples in Φ_2 functions for test modules A, B and C in the range of separation distance $0.1 \leqslant S/D_j \leqslant 8$. It is worth noting that, an increase of Φ_2 function value shown in Fig. 10 physically implies an enhancing dominance of *Re* impact on heat transfer because the Φ_2 value can be treated as the index to quantify the influences of *Re* effects on the overall convection. The varying features of Φ_2 values shown in Fig. 10 suggest that the dominance of *Re* impact varies with S/D_j, the controlled area defined (Nu_a or Nu_c) and the jet-array tested. It is interesting to note, only for test array C, the curving natures for the Φ_s-functions of Nu_a and Nu_c in the S/D_j range where the ripples occur are opposite in mirror. The S/D_j range where *Re* impact dominates the Nu_a values corresponds with minor *Re* effect on Nu_c when the Φ_s-function plots of Nu_a and Nu_c for test array C are compared. Relative to the Φ_s–S/D_j relationships typified in Fig. 10 for jet-arrays B and C, the variations of Φ_s-function for test module A are much more insensitive to the change of S/D_j value. Justified by this regression-type evidence, the coupling *Re*–S/D_j effects are enhanced when the orifices with different diameters organize a jet array.

The overall success of the proposed correlations embodied in Eqs. (2) to (3) for Nu_a and Nu_c over the impinging surfaces of jet-arrays A, B and C is examined by comparing all the experimental measurements with the empirical predictions as indicated in Fig. 11. As shown in Fig. 11, the values of Nu_a and Nu_c indicating by the ranges of data spreads with test module C are generally higher. The maximum discrepancy of ±20% between the experimental and correlative results is achieved for 95% of the entire set of data. Even with the presence of groove-induced complexities for an array fitted with non-equal-diameter orifices, the experimentally based correlations could still offer the reasonable predictions for Nu_a and Nu_c.

4. Conclusions

The detailed heat transfer measurements of three impinging jet arrays issued from grooved orifice plates are performed to study the combined effects of groove and nozzle-size distribution on heat transfer with various S/D_j and *Re* values. The vertical groove on orifice plate and the variable distributions nozzle-sizes in a jet-array have demonstrated their impacts on the local and area-averaged heat transfers due to their effects on the inter-jet reactions which involve the enhanced or weakened jet momentum and the modified wall-jet flows. These mechanisms through which the variations of S/D_j or *Re* modify the heat transfers are inter-related that leads to the presence of coupling S/D_j–*Re* effects. In conformity with the experimental evidences, a regression-type analysis is formulated to derive the empirical heat transfer correlations that permit the evaluations of isolated and interactive effects of S/D_j and *Re* on Nu_a and Nu_c. The salient points that have been identified are as follows.

(1) With very small separation distances ($S/D_j < 1$), the heat transfer improvement among the most confined central jet region in a jet-array is attainable by ejecting jets from the grooved surface. This measure not only provides favorable treatment of spent fluids but the deflected jets confined in the groove could also enrich the central-jet momentum via the enhanced entrainment at small separation distance. A net result is the heat transfer augmentation over the central-jet region in the array. At $0.1 S/D_j$, the stagnant Nusselt number

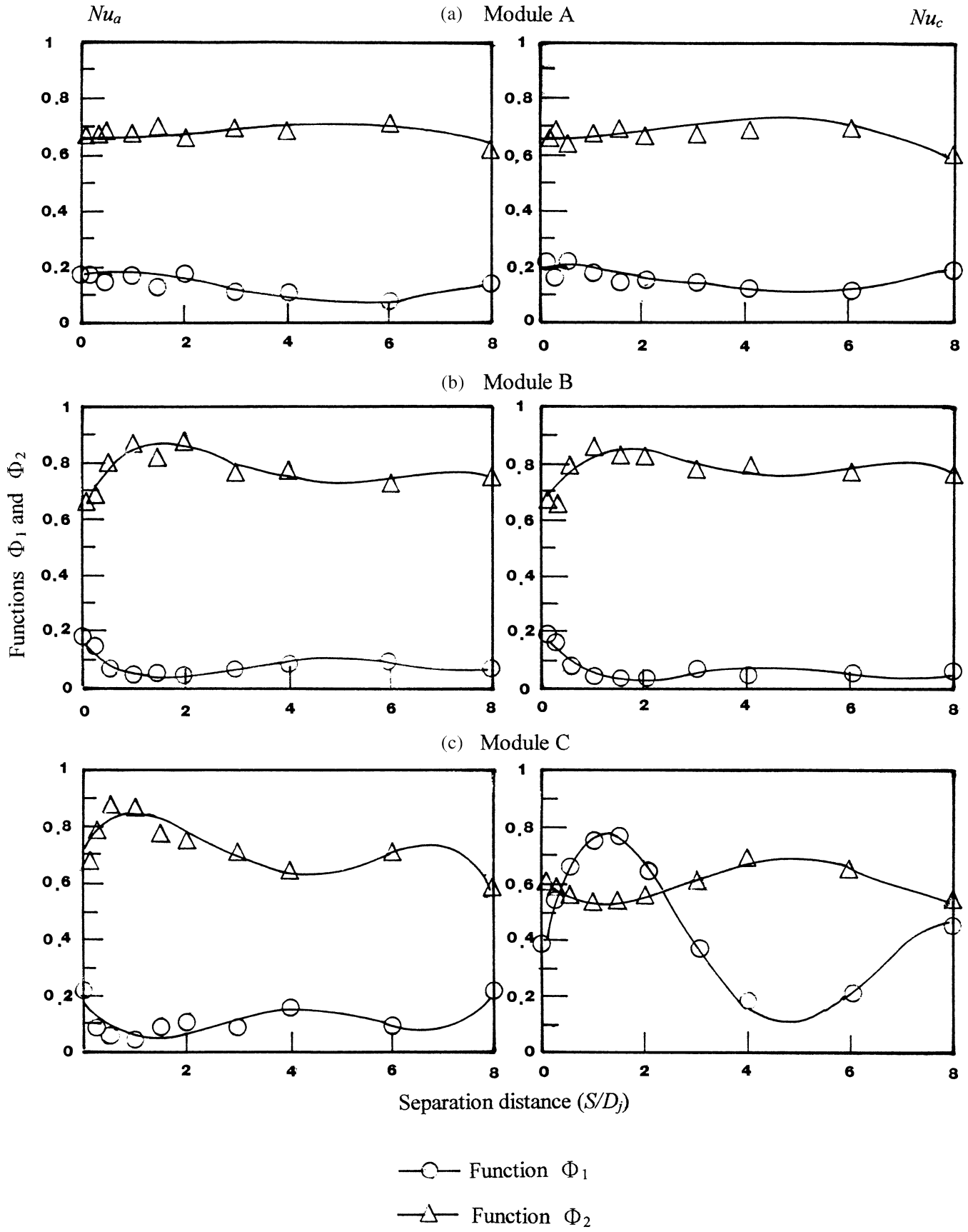

Fig. 10. Comparison of polynomial curve fits for functions Φ_1 and Φ_2 with experimental data.

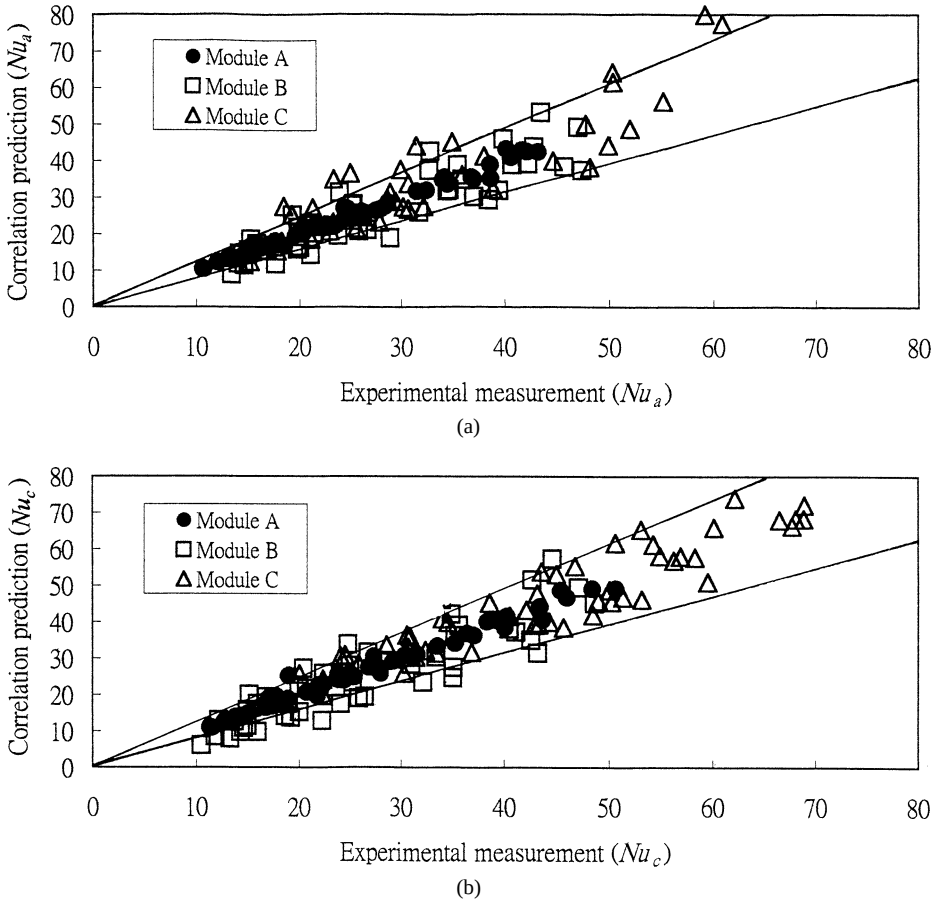

Fig. 11. Comparison of experimental measurements with correlated results: (a) Spatially averaged Nusselt number over impinging surface. (b) Spatially averaged Nusselt number over central jet region.

of central jet issued from the grooved orifice plate could be increased to about 115% of the corresponding level obtained with the smooth-walled orifice plate.

(2) Owing to the presence of groove, the jet-to-jet interactions prior to and after impingement vary spatially and are sensitive to both nozzle-size distribution and separation distance. Depending on the values of *Re*, S/D_j and the jet configuration, a variety of Nusselt number distributions over the impinging surfaces are revealed. In test array A, the confinement provided by the side-column jets impedes the heat transfer over the central-column region with $S/D_j > 1$; while the groove effect enriches the momentums of central-column jets that improves the regional heat transfers with $S/D_j < 1$. In test array B, the cooling performances for the central and side column-jets are respectively undermined and improved from the baseline scenarios. The identities of central-column jets disappear in test array B when $S/D_j > 4$. With $S/D_j < 1$, although the groove effect still prevails in test array B, the enhanced central-column jet-momentum over the groove region is accompanied by the stronger inter-jet confinements. In test array C, the central-column jets always remain as the most effective cooling elements over the range of $0.1 \leqslant S/D_j \leqslant 8$. The increments of stagnant Nusselt numbers over the central-column region in test array C reach about 50–95% of the baseline levels. To accommodate the locally high cooling duty, the arrangement of orifices with the larger diameters in the grooved surface is demonstrated as a feasible approach.

(3) The optimal S/D_j value that produces the highest Nu_a or Nu_c depend on *Re* and jet-array configuration. Because Φ_2 values in Nu_a and Nu_c correlations are different and vary with S/D_j, the dominance of *Re* effect on heat transfer varies with S/D_j and are spatially dependent, especially when the non-equal-diameter jets organize the jet-array. Led by the overall review of all $Nu_{a,c}$–S/D_j plots generated, test array C generally offers the highest Nu_a and Nu_c values among the three test arrays in the range of $0.1 < S/D_j < 2$.

(4) The proposed Nu_a and Nu_c correlations are consistent with the experimentally revealed heat transfer physics that permit the individual and interactive effects of jet Reynolds number and separation distance on heat transfer for the test modules A, B and C to be evaluated.

References

[1] R.N. Koopman, E.M. Sparrow, Local and average transfer coefficients due to an impinging rows of jets, Internat. J. Heat Mass Transfer 19 (1976) 673–683.

[2] H. Martin, Heat and mass transfer between impinging gas jets and solid surfaces, Adv. Heat Transfer 8 (1977) 1–60.

[3] L.W. Florschuetz, C.R. Truman, D.E. Metzger, Streamwise flow and heat transfer distribution for jet impingement with crossflow, ASME J. Heat Transfer 103 (2) (1981) 337–342.

[4] N. Obot, T.A. Trabold, Impingement hea transfer within arrays of circular jets. Part I: Effects of minimum, intermediate, and complete crossflow for small and large spacings, ASME J. Heat Transfer 109 (4) (1987) 872–879.

[5] R.J. Goldstein, W.S. Seol, Heat transfer to a row of impinging circular air jets including the effect of entrainment, Internat. J. Heat Mass Transfer 34 (1991) 2133–2147.

[6] D.K. Lee, K. Vafai, Comparative analysis of jet impingement and microchannel cooling for high heat flux application, Internat. J. Heat Mass Transfer 42 (1999) 1555–1568.

[7] D.E. Metzger, R.J. Korstad, Effects of crossflow on impingement heat transfer, ASME J. Engrg. Power 94 (1972) 35–42.

[8] L.W. Florschuetz, R.A. Berry, D.E. Metzger, Periodic streamwise variation of heat transfer coefficients for inline and staggered arrays of circular jets with crossflow of spent air, ASME J. Heat Transfer 102 (1) (1980) 132–137.

[9] L.W. Florschuetz, D.E. Metzger, C.C. Su, Y. Isoda, H.H. Tseng, Heat transfer characteristics for jet array impingement with initial crossflow, ASME J. Heat Transfer 106 (1) (1984) 34–41.

[10] Y. Huang, S.V. Ekkad, J.C. Han, Detailed heat transfer distributions under an array of orthogonal impinging jets, J. Thermophys. Heat Transfer 12 (1) (1998) 73–79.

[11] B.R. Hollworth, L. Dagan, Arrays of impinging jets with spent fluid removal through vent holes on the target surface—Part I: Average heat transfer, ASME J. Engrg. Power 102 (1980) 994–999.

[12] A.M. Huber, R. Viskanta, Convective heat transfer to a confined impinging array of air jets with spent air exits, ASME J. Heat Transfer 116 (1994) 570–576.

[13] A.M. Huber, R. Viskanta, Effect of jet-to-jet spacing on convective heat transfer to confined, impinging arrays of axisymmetric air jets, Internat. J. Heat Mass Transfer 37 (18) (1994) 2859–2869.

[14] Y. Pan, B.W. Webb, Heat transfer characteristics of arrays of free-surface liquid jets, ASME J. Heat Transfer 117 (1995) 878–883.

[15] R. Gardon, J.C. Akfirat, Heat transfer characteristics of impinging two-dimensional air jets, ASME J. Heat Transfer 88 (1966) 101–108.

[16] M. Korger, F. Krizek, Mass transfer coefficient in impingement flow from slotted nozzles, Internat. J. Heat Mass Transfer 9 (1966) 337–344.

[17] A.I. Behbahani, R.J. Goldstein, Local heat transfer to staggered arrays of impinging circular air jets, ASME J. Engrg. Power 105 (1983) 354–360.

[18] S. Polat, B. Huang, A.S. Mujumbar, W.J.M. Douglas, Numerical flow and heat transfer under impinging jets: A review, in: C.L. Tien (Ed.), Annual Review of Numerical Fluid Mechanics and Heat Transfer, Vol. 2, Hemisphere, Washington, DC, 1989, pp. 157–197.

[19] Editorial Board of ASME J. Heat Transfer, Journal of heat transfer policy on reporting uncertainties in experimental measurements and results, ASME J. Heat Transfer 115 (1993) 5–6.

[20] S.W. Chang, Y. Zheng, Heat transfer of impinging jets arrays, Internat. J. Exp. Heat Transfer, 2001, submitted.